

Electrical conductivity of warm neutron star crust in magnetic fields: Neutron-drip regime

Arus S. Harutyunyan,^{1,2,*} Armen Sedrakian,^{3,4,†} Narine T. Gevorgyan,^{1,5,‡} and Mekhak V. Hayrapetyan^{2,§}

¹*Byurakan Astrophysical Observatory, Byurakan 0213, Armenia*

²*Department of Physics, Yerevan State University, Yerevan 0025, Armenia*

³*Frankfurt Institute for Advanced Studies, D-60438 Frankfurt am Main, Germany*

⁴*Institute of Theoretical Physics, University of Wrocław, 50-204 Wrocław, Poland*

⁵*A.I. Alikhanyan National Science Laboratory (Yerevan Physics Institute), Yerevan, Armenia*

We compute the anisotropic electrical conductivity tensor of the inner crust of a compact star at non-zero temperature by extending a previous work on the conductivity of the outer crust. The physical scenarios, where such crust is formed, involve proto-neutron stars born in supernova explosions, binary neutron star mergers and accreting neutron stars. The temperature-density range studied covers the transition from a non-degenerate to a highly degenerate electron gas and assumes that the nuclei form a liquid, *i.e.*, the temperature is above the melting temperature of the lattice of nuclei. The electronic transition probabilities include (a) the dynamical screening of electron-ion interaction in the hard-thermal-loop approximation for the QED plasma, (b) the correlations of the ionic component in a one-component plasma, and (c) finite nuclear size effects. The conductivity tensor is obtained from the Boltzmann kinetic equation in relaxation time approximation accounting for the anisotropies introduced by a magnetic field. The sensitivity of the results towards the matter composition of the inner crust is explored by using several compositions of the inner crust which were obtained using different nuclear interactions and methods of solving the many-body problem. The standard deviation of relaxation time and components of the conductivity tensor from the average are below $\leq 10\%$ except close to crust-core transition, where non-spherical nuclear structures are expected. Our results can be used in dissipative magneto-hydrodynamics (MHD) simulations of warm compact stars.

I. INTRODUCTION

The knowledge of transport properties of hot baryonic matter is important for large-scale magneto-hydrodynamics description of astrophysical phenomena associated with compact stars. One such setting offer the binary neutron star (BNS) mergers: matter is expected to be heated both in the post-merger and pre-merger phases. In the post-merger phase, the matter is heated to temperatures of the order of several tens of MeV by deposition of kinetic and gravitational energy in the matter; in the pre-merger phase, the matter may be heated via the dissipation of the energy of the tidally induced oscillations. Another longer time-scale setting is offered by the accreting neutron stars as their crusts are heated through the infalling matter and the onset of nuclear reactions in various crustal layers. The warm matter regime is of interest also in the context of transient proto-neutron stars born in supernova explosions.

Transport in compact star plasma has been extensively studied in the cold and dense limit where it is dominated by the degenerate fermionic quantum liquids over a long period of time; for general reviews see [1, 2]. More recently, the electrical conductivity of the warm outer crust was computed in Ref. [3] in the context of BNS mergers; it also provides a detailed review of the previous work on the conductivity of crustal matter in the cold regime, which we do not repeat here. The conductivity tensor of Ref. [3] was then used to assess its importance in the dynamics of BNS mergers [4], showing the

conditions for the breakdown of the ideal MHD limit and the importance of the Hall conductivity.

This paper extends a previous calculation of the conductivity of heated crustal matter in non-quantizing magnetic fields [3] to the inner crust phase where along with the crustal lattice, there is an unbound neutron component. Our focus is on the case with spherical nuclei for which several compositions computed in Refs. [5–8] will be used. The conductivity of pasta phases where the shapes and topologies of nuclei deviate strongly from the spherical within the layer between the stellar core and the phase with spherical nuclei was studied in Ref. [9]. We will restrict our discussion to magnetic fields below $B_c \approx 10^{14}$ G. Above these values, the Landau quantization of electron trajectories must be taken into account, see Ref. [10].

Among the other finite-temperature transport coefficients, the bulk viscosity appears to play a particularly important role (even in the absence of the magnetic field) as it follows from the initial estimates [11] and subsequent microscopic computations [12, 13]. These were followed by the estimates of relevant damping timescales [14, 15] and implementations in the hydrodynamics simulations [16, 17].

The paper is organized as follows. In Sec. II we review the compositions of the neutron star’s inner crust which are used in our computations of the electrical conductivity tensor. Section III collects the relevant ingredients of the formalism and key results, which have been presented in detail in Ref. [3]. Our numerical results are discussed in Sec. IV. The final section V contains a summary of our results.

We use the natural (Gaussian) units with $\hbar = c = k_B = 1$, $e = \sqrt{\alpha}$, $\alpha = 1/137$ and the metric signature $(1, -1, -1, -1)$.

* arus@bao.sci.am

† sedrakian@fias.uni-frankfurt.de

‡ gevorgyan.narine@gmail.com

§ mhayrapetyan@ysu.am

II. EQUATION OF STATE, COMPOSITION AND PHYSICAL CONDITIONS IN INNER CRUST

Above the neutron drip density $\rho_{\text{drip}} = 4.3 \times 10^{11} \text{ g cm}^{-3}$ a phase transition takes place in neutron star crusts: the low-density phase consisting of fully ionized nuclei and relativistic electrons is replaced by a phase which in addition to the components of the low-density phase has also unbound neutrons. Then, the total baryon density n_B is given by

$$n_B = An_i + n_n, \quad (1)$$

where n_i is the number density of the ions (nuclei) and n_n is the number density of unbound neutrons. The nuclei are characterized by their nucleon number A and proton number Z . The ion-electron sub-system, viewed as Coulomb plasma, is characterized by the parameters

$$\Gamma = \frac{T_C}{T}, \quad T_C = \frac{e^2 Z^2}{a_i}, \quad (2)$$

where e is the elementary charge, T is the temperature, $a_i = (4\pi n_i/3)^{-1/3}$ is the radius of the spherical volume per ion. For $\Gamma \ll 1$ ($T \gg T_C$) ions are weakly coupled and because of their large mass they form a classical Boltzmann gas. When $\Gamma \geq 1$ ions are strongly coupled and form a solid phase with nuclei arranged in a regular lattice for $\Gamma > \Gamma_m \simeq 160$. In the opposite case $\Gamma < \Gamma_m$ the liquid phase is energetically preferred. The temperature of melting of the crustal lattice is given by $T_m = T_C/\Gamma_m$. The lattice plasma temperature is defined as

$$T_p = \left(\frac{4\pi Z^2 e^2 n_i}{M} \right)^{1/2}, \quad (3)$$

where M is the ion mass. (Note that in units where $\hbar = 1$, the plasma frequency and plasma temperature coincide). The quantum regime for ion lattice (under which the quantization of oscillations of the lattice is required) occurs for $T \leq T_p$.

For numerical computations, we will adopt five different density-dependent compositions of stellar matter for the inner crust of a neutron star, which we label as NV [5], DIM and DIM* [6], Bsk24 [7] and Sly9 [8]. The compositions that we will use were computed at $T = 0$. We will assume below that the composition does not depend strongly on the temperature in the range of temperatures studied here so that the background composition of the inner crust in each case will be fixed at the one derived for $T = 0$. The physical conditions change significantly with the increasing temperature at about $T_{\text{tr}} \simeq 5 \text{ MeV}$ where the neutrinos become trapped and β -equilibrium conditions are changed. As the temperature is further increased the appearance of lighter clusters – deuterons, tritons, helions, and alpha-particles become possible for temperatures $T \geq 10 \text{ MeV}$ [18–23]. Their contribution to conductivity is left for future study.

Figure 1 shows the proton number Z and the nucleon number A of the nuclei as functions of the net mass density for the chosen compositions of the stellar matter. Up to densities $\log \rho [\text{g cm}^{-3}] \leq 13$ all predict $Z = 40$ semi-magic proton values. Above these densities, Bsk24 and DIM* predict

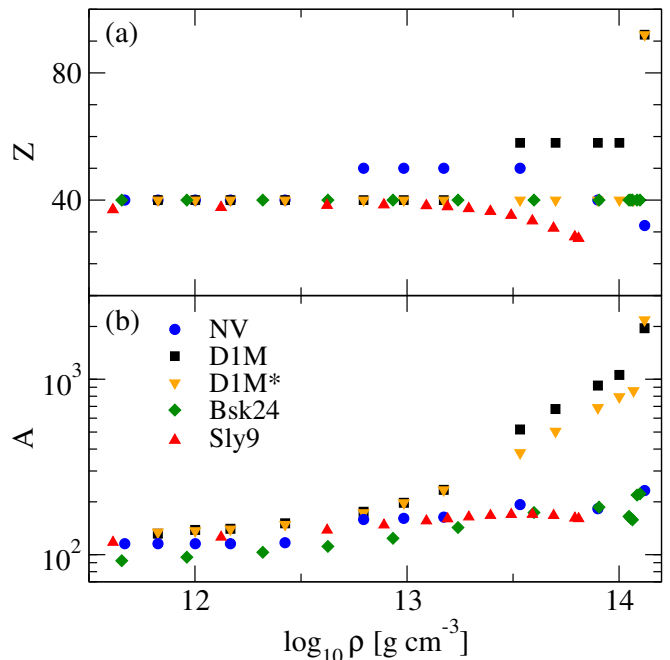


FIG. 1. The proton number Z (upper panel) and the nucleon number A (lower panel) of the nuclei as functions of the mass density for five different compositions of the stellar matter labeled as NV [5], DIM and DIM* [6], Bsk24 [7], and Sly9 [8].

the same $Z = 40$ value, NV composition predicts the magic value $Z = 50$ (except the last point) whereas DIM and Sly predict higher and lower Z values, respectively. Therefore, the scattering matrix elements for the electron scattering off the individual nuclei are nearly the same for these compositions at low densities but deviate at higher densities. However, since the transport depends on the average number of nuclei per unit value, such factors as the free neutron density and the mass number of a nucleus are important, see Eq. (1), which non-trivially modify the predictions based on the value of Z .

Figure 2 shows the fraction of free neutrons and the ion number density as functions of the mass density for all five compositions studied. Notable deviations are seen in the high-density range $13 \leq \log \rho [\text{g cm}^{-3}] \leq 14$, where the models NV and Sly9 predict smaller nuclei and large neutron fraction ($n_n/n_B \geq 90\%$) than the remaining models ($n_n/n_B \lesssim 80\%$).

Figure 3 shows the phase diagram of the matter in the inner crust of neutron stars in the temperature-density plane for five compositions. In the upper part of the diagram where $T > T_C$ the ionic component forms a weakly interacting Boltzmann gas, as the thermal energy exceeds the Coulomb interaction energy. In the lower part of the diagram where $T < T_m$ the ionic component solidifies, *i.e.*, the scattering of electrons is (predominantly) on the phonons of the lattice. The plasma temperature T_p is lower than the melting temperature for the five models in Fig. 3 and is not shown. Our results apply in the regime where $T > T_m$. Note the weak density and model dependence of the curves $T_m(\rho)$ and $T_C(\rho)$.

The transport in the liquid phase of a neutron star's inner

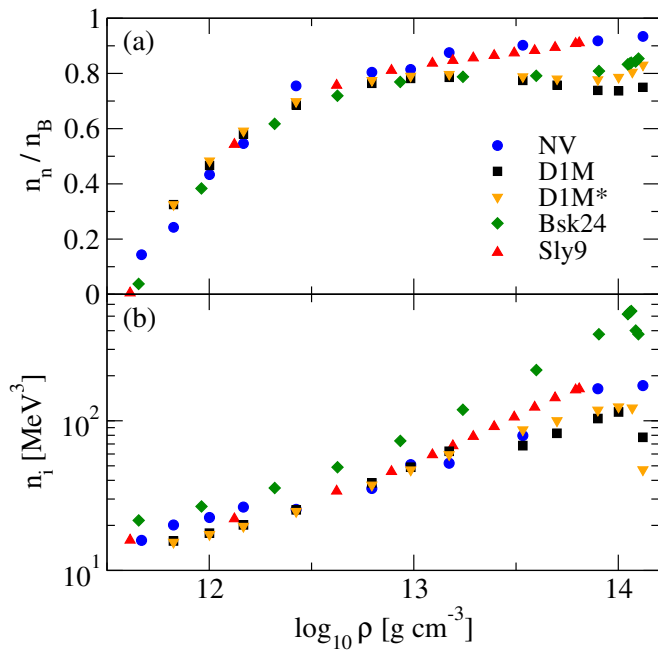


FIG. 2. The fraction of free neutrons (a) and the number density of ions (b) as functions of the mass density for five compositions of stellar matter.

crust is controlled by the electrons which, to a good approximation, can be treated as a free Fermi gas except for the collisions with ions that lead to dissipation contributing to conductivity. (Electron-electron interaction can affect the conductivity indirectly by modifying the density of state of electrons, but the correction is a higher order effect in the fine structure constant). The electron density is obtained from the charge conservation $n_e = Zn_i$ and allows us to define their low-temperature characteristics, such as Fermi energy $\varepsilon_F = (p_F^2 + m^2)^{1/2}$ and temperature $\varepsilon_F - m \equiv T_F$, where m is the electron mass and $p_F = (3\pi^2 n_e)^{1/3}$ is the Fermi momentum. Note that at densities considered in this paper electrons are ultrarelativistic therefore we have, in practice, $T_F = \varepsilon_F = p_F$.

The Fermi temperature for five compositions is shown in Fig. 4. It is seen that electrons are degenerate up to a quite high temperature of several tens of MeV. This is in contrast to the outer crust region [3], where low densities required treatment of the transition from degenerate to the non-degenerate regime. Nevertheless, as our set-up works across from non-degenerate to strongly degenerate limits, no additional limitations are imposed. Note the large differences in the Fermi energies predicted by the Bsk24 and remaining models, which arise from a combination of factors. For example, this difference when compared to the NV model arises from the differences in the free-neutron fraction and, consequently, the number of ions per unit volume despite similar values of predicted Z values. Overall, we see that electrons are degenerate or semi-degenerate for the temperatures relevant to BNS mergers and core-collapse supernovas at densities relevant to compact star inner crust. We recall that our discussion is lim-

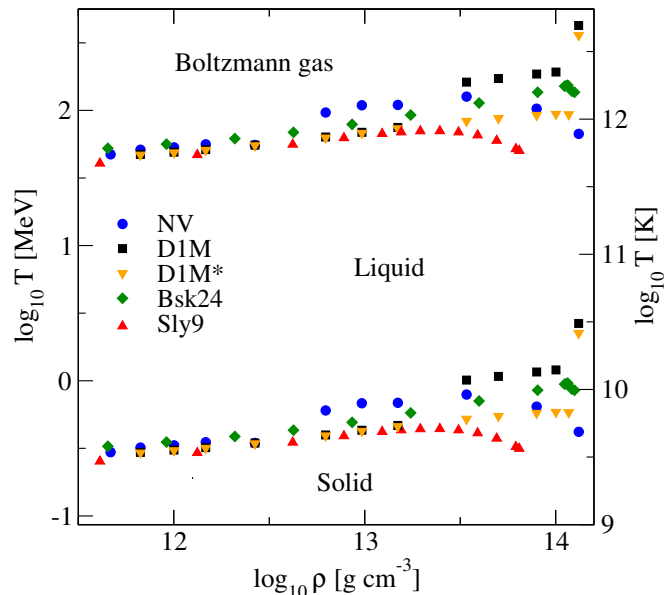


FIG. 3. The phase diagram of dense plasma in the inner crust of the neutron star in the temperature-density plane for five different compositions. The lower curves show the melting temperature T_m below which the ionic component solidifies. Upper curves show T_C above which the ionic component forms a Boltzmann gas. The present study covers the liquid portion of the phase diagram.

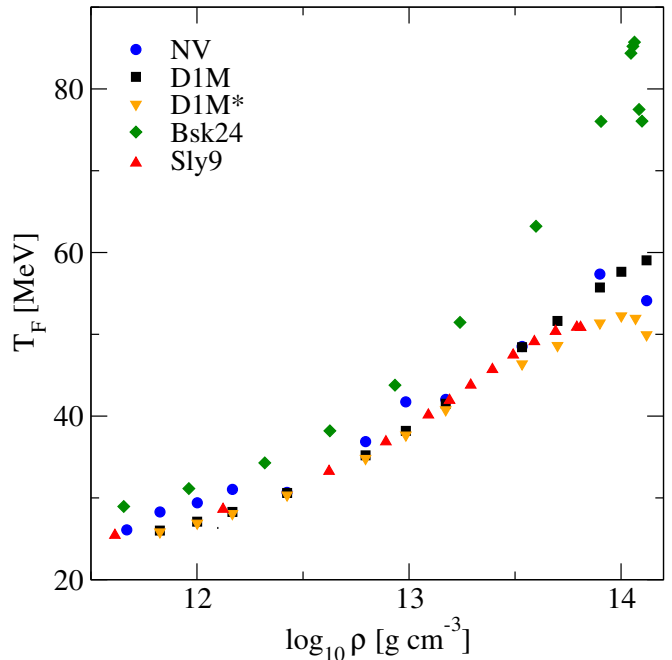


FIG. 4. The Fermi temperature T_F of the electronic component of the stellar matter in the inner crust of a neutron star for five different compositions shown in Fig. 1. The electron gas is becoming gradually non-degenerate above and degenerate below this temperature.

ited to temperatures below several MeV, as the compositions

adopted will be modified due to finite temperature effects at larger temperatures. In addition, to modifications of thermodynamics, additional species such as alpha particles and other light clusters will appear in the matter [18–23] and will contribute to the conductivity. As a consequence, we will focus on the degenerate electron regime while providing some extrapolation to higher temperatures which are suggestive of the behavior of various quantities.

III. CONDUCTIVITY IN MAGNETIC FIELD FROM BOLTZMANN EQUATION

In this section, we provide the key ingredients of the formalism presented extensively in Ref. [3] which is based on the (quasi)particle transport of electrons in strong magnetic fields. The kinetics of electrons is described by the Boltzmann equation for the electron distribution function

$$\frac{\partial f}{\partial t} + \mathbf{v} \frac{\partial f}{\partial \mathbf{r}} - e(\mathbf{E} + [\mathbf{v} \times \mathbf{H}]) \frac{\partial f}{\partial \mathbf{p}} = I[f], \quad (4)$$

where \mathbf{E} and \mathbf{H} are the electric and magnetic fields, \mathbf{v} is the electron velocity, e is the unit charge, and $I[f]$ is the collision integral, which for electron-ion collisions has the form

$$I = -(2\pi)^4 \sum_{234} |\mathcal{M}_{12 \rightarrow 34}|^2 \delta^{(4)}(p + p_2 - p_3 - p_4) \times [f(1 - f_3)g_2 - f_3(1 - f)g_4], \quad (5)$$

where $f = f(p)$ and $f_3 = f(p_3)$ are the distribution functions of the incoming and outgoing electron, $g_{2,4} = g(p_{2,4})$ are the distribution functions of the ion before and after a collision, and we introduced the short-hand notation: $\sum_i = \int d\mathbf{p}_i / (2\pi)^3$.

As discussed above, ions form a classical liquid in equilibrium with the Maxwell-Boltzmann distribution, *i.e.*,

$$g(p) = n_i \left(\frac{2\pi}{MT} \right)^{3/2} \exp\left(-\frac{p^2}{2MT}\right). \quad (6)$$

Below we will consider small perturbations δf around the equilibrium Fermi-Dirac distribution function of electrons to linearize the Boltzmann equation: $f = f^0 + \delta f$, $\delta f \ll f_0$, where the equilibrium distribution is given by

$$f^0(\varepsilon) = \frac{1}{e^{(\varepsilon - \mu)/T} + 1}, \quad (7)$$

with the spectrum of non-interacting electrons given by $\varepsilon = \sqrt{p^2 + m^2}$, and μ is the electron chemical potential. Since we are interested in the electrical conductivity we keep only the last term on the left-hand side of Eq. (4). Substituting the $f = f^0 + \delta f$ in Eq. (4) and decomposing δf in terms of independent tensor components containing the electric and magnetic fields we obtain [3]

$$\delta f = \frac{e\tau}{1 + (\omega_c\tau)^2} \frac{\partial f^0}{\partial \varepsilon} v_i \left[\delta_{ij} - \omega_c\tau \varepsilon_{ijk} b_k + (\omega_c\tau)^2 b_i b_j \right] E_j, \quad (8)$$

where $\mathbf{b} \equiv \mathbf{B}/B$, $\omega_c = eB/\varepsilon$ is the cyclotron frequency for electrons, and the Latin indices label the components of Cartesian coordinates. Here we work in the relaxation-time approximation with the relaxation time defined by

$$\tau^{-1}(\varepsilon) = (2\pi)^{-5} \int d\mathbf{q} \int d\mathbf{p}_2 |\mathcal{M}_{12 \rightarrow 34}|^2 \frac{\mathbf{q} \cdot \mathbf{p}}{p^2} \times \delta(\varepsilon + \varepsilon_2 - \varepsilon_3 - \varepsilon_4) g_2 \frac{1 - f_3^0}{1 - f^0}. \quad (9)$$

The electrical conductivity is then obtained by computing the electrical current

$$j_i = -2 \int \frac{d\mathbf{p}}{(2\pi)^3} e v_i \delta f = \sigma_{ij} E_j. \quad (10)$$

Substituting Eq. (8) in Eq. (10) and we find

$$\sigma_{ij} = \delta_{ij} \sigma_0 - \varepsilon_{ijm} b_m \sigma_1 + b_i b_j \sigma_2, \quad (11)$$

where

$$\sigma_n = \frac{e^2}{3\pi^2 T} \int_m^\infty d\varepsilon \frac{p^3}{\varepsilon} \frac{\tau(\omega_c\tau)^n}{1 + (\omega_c\tau)^2} f^0(1 - f^0), \quad n = 0, 1, 2. \quad (12)$$

The matrix element includes several corrections to the bare Coulomb interaction between an electron and an ion. The screening of the interaction is taken into account via the hard-thermal-loop polarization tensor of QED, see Sec. IV D of Ref. [3]. The ion-ion correlations are taken by using fits to the structure factor $S(q)$ of one-component plasma for various values of plasma parameter Γ obtained from Monte Carlo computations, see Fig. 4 of Ref. [3]. Finally, the finite nuclear size of the nuclei is taken into account via a nuclear form factor $F(q)$ given by Eq. (31) of the same reference. The final expression reads

$$\tau^{-1}(\varepsilon) = \frac{\pi Z^2 e^4 n_i}{\varepsilon p^3} \sqrt{\frac{M}{2\pi T}} \int_{-\infty}^{\varepsilon - m} d\omega e^{-\omega/2T} \frac{f^0(\varepsilon - \omega)}{f^0(\varepsilon)} \times \int_{q_-}^{q_+} dq (q^2 - \omega^2 + 2\varepsilon\omega) \frac{(2\varepsilon - \omega)^2 - q^2}{|q^2 + \Pi_L|^2} \times e^{-\omega^2 M/2q^2 T} e^{-q^2/8MT} S(q) F^2(q), \quad (13)$$

where $q_{\pm} = \left| \sqrt{p^2 - (2\omega\varepsilon - \omega^2) \pm p} \right|$, and $\Pi_L \simeq 4e^2 p_F^2 / \pi$ is the longitudinal component of the polarization tensor. Note that we neglected the transverse part of the scattering in Eq. (13) as that part is negligibly small in the regime of interest of this work.

If the magnetic field is directed along the z -axis, then the conductivity tensor has the form

$$\hat{\sigma} = \begin{pmatrix} \sigma_0 & -\sigma_1 & 0 \\ \sigma_1 & \sigma_0 & 0 \\ 0 & 0 & \sigma \end{pmatrix}, \quad (14)$$

where the scalar conductivity is given by

$$\sigma = \sigma_0 + \sigma_2 = \frac{e^2}{3\pi^2 T} \int_m^\infty d\varepsilon \frac{p^3}{\varepsilon} \tau f^0(1 - f^0). \quad (15)$$

In the absence of a magnetic field, the conduction becomes isotropic with $\mathbf{j} = \sigma \mathbf{E}$, where σ is referred below as scalar conductivity.

As the electronic gas in the inner crust is practically always in the degenerate state, we can use the low-temperature limit of Eqs. (12) and (15) by substituting $\partial f^0/\partial \varepsilon = -f^0(1 - f^0)/T \rightarrow -\delta(\varepsilon - \varepsilon_F)$, which leads us to the well-known Drude formulae

$$\sigma = \frac{n_e e^2 \tau}{\varepsilon_F}, \quad \sigma_0 = \frac{\sigma}{1 + (\omega_c \tau)^2}, \quad \sigma_1 = (\omega_c \tau) \sigma_0, \quad (16)$$

where the relaxation time and the cyclotron frequency should be evaluated at the Fermi energy as well, *i.e.*, $\tau = \tau(\varepsilon_F)$ and $\omega_c = eB/\varepsilon_F$.

IV. NUMERICAL RESULTS

Numerically, the electrical conductivity is evaluated using the relaxation time Eq. (13). With this relaxation time, we evaluate the components of the conductivity tensor using Eq. (12). Two different regimes of weak and strong magnetic fields arise which are distinguished by the scalar vs. tensor nature of the conductivity, see Eq. (16). These regimes are distinguished by the value of *anisotropy parameter* $\omega_c \tau$. In the isotropic case $\omega_c \tau \ll 1$ one has $\sigma_1 \ll \sigma_0 \simeq \sigma$, therefore, all three diagonal components of the conductivity tensor are identical, and the non-diagonal components vanish. In the anisotropic case $\omega_c \tau \simeq 1$ they are distinct and should be studied separately. Below, we will study the dependence of the conductivity on the density, temperature, and strength of the magnetic field for the selected compositions.

A. Relaxation time and anisotropy parameter

Figure 5 shows the relaxation time τ and the product $\omega_c \tau$ for five compositions as functions of the mass density. The temperature is fixed at $T = 3$ MeV, which corresponds to the degenerate regime of stellar matter, therefore τ and ω_c are evaluated at the Fermi energy.

The variations in the relaxation time and anisotropy parameter $\omega_c \tau$ with the composition can be understood from the scalings of these quantities with Z , A , n_i , etc. Since the low-temperature limit is realized in the inner crust, we use a simplified version of (13) given in this limit by [3, 24]

$$\tau^{-1} = \frac{4Ze^4 \varepsilon_F}{3\pi} \int_0^{2p_F} \frac{dq}{q} \left(1 - \frac{q^2}{4\varepsilon_F^2}\right) S(q) F^2(q), \quad (17)$$

which implies the scaling

$$\tau^{-1} \sim Z^{4/3} n_i^{1/3} \sim Z^{4/3} \left(\frac{n_B - n_n}{A}\right)^{1/3}, \quad (18)$$

where we used $\varepsilon_F = p_F \sim (Zn_i)^{1/3}$. The dependence of the relaxation time on the characteristics of nuclei predicted by the composition obeys thus the scaling to $\tau \sim Z^{-4/3} A^{1/3}$. Because the value of Z for most of the compositions is fixed at

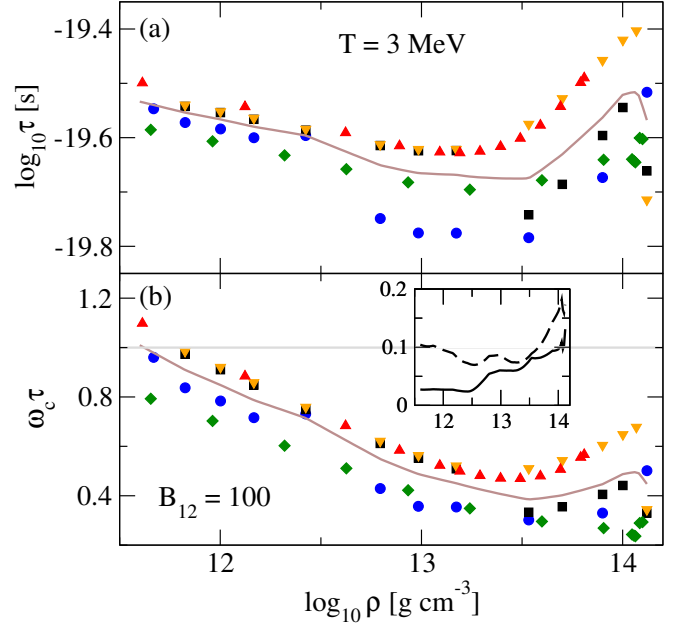


FIG. 5. The relaxation time τ and the product $\omega_c \tau$ as functions of the mass density for five compositions as labeled in Fig. 1. The temperature is fixed at $T = 3$ MeV, and the magnetic field is fixed at $B_{12} = 100$ for panel (b). The solid lines show the values of these quantities averaged over the five compositions. The solid and dashed curves in the inset show the standard deviations of $\log \tau$ and $\omega_c \tau$, respectively.

(semi)-magic number 40 or 50, the variations of the relaxation time with composition is mainly due to the dependence on the mass number of nuclei. At densities $\log \rho [\text{g cm}^{-3}] > 13$ the difference in the free neutron gas density (which could become significant) affects the relaxation time as well. For example, at $\log \rho [\text{g cm}^{-3}] \geq 13.5$ the relaxation time becomes a slowly increasing function of the mass density for models DIM and DIM* as these models predict a significant increase in the mass number of nuclei with the density in this high-density regime, as seen from Fig. 1. For the compositions NV and Sly9, which are characterized by almost constant values of A , the increase of the relaxation time in the high-density regime is mainly due to the fast increase of the free neutron fraction in this regime, which leads to smaller ion and electron number densities and, therefore, to smaller electron-ion scattering amplitudes. In the case of Sly9 the relaxation times are large because of the additional effect of decreasing Z -values at high densities not seen in any other composition. Note that the non-monotonic behavior of the relaxation time found here is in contrast to the results obtained in Ref. [3] for outer-crust-matter, where the relaxation time was always a decreasing function of the density, as suggested also by the scaling (18) $\tau \sim n_B^{-1/3}$.

The solid line in panel (a) of Fig. 5 shows the average logarithmic relaxation timescale computed as $\langle \log \tau \rangle = \sum_{i=1}^5 \log \tau_i / 5$, where τ_i are the relaxation times for the five compositions interpolated in the density range $11.6 \leq$

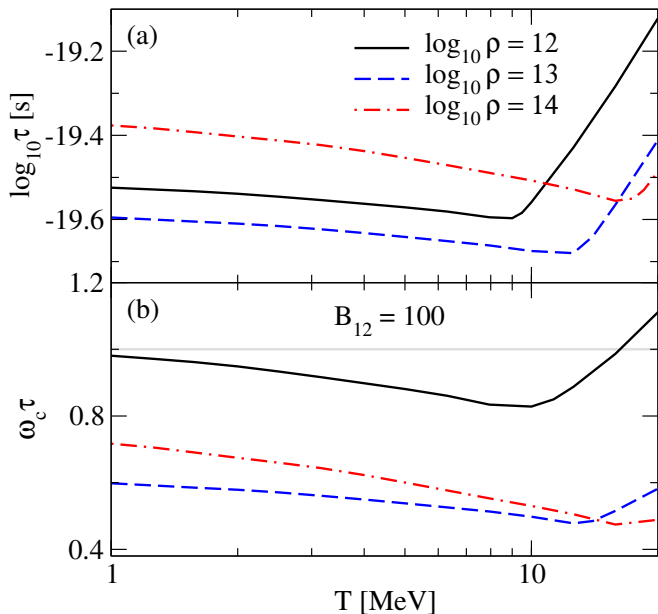


FIG. 6. The relaxation time τ and the product $\omega_c \tau$ as functions of the temperature for various values of the mass density for composition DIM*. In panel (b) the magnetic field is fixed at $B_{12} = 100$.

$\log \rho [\text{g cm}^{-3}] \leq 14.12$. Similarly, the solid line in panel (b) shows the average value of $\omega_c \tau$. In addition, we show the standard deviations of these quantities from their average values in the inset located in panel (b) of Fig. 5. The solid line shows the standard deviation for $\log \tau$, and the dashed line – that for $\omega_c \tau$. We compute the standard derivation s_a of a quantity a using the formula $s_a = \sqrt{\sum_{i=1}^5 (a_i - \langle a \rangle)^2 / 5}$, where $\langle a \rangle$ is the average value over the five compositions.

Figure 6 shows the temperature dependence of the relaxation time and the product $\omega_c \tau$ for several densities for the composition DIM*. Here we extrapolate our results of low-temperature matter to higher temperatures (up to 20 MeV) making a crude assumption that the composition of matter does not change significantly with the temperature at the given density. As the matter is partially degenerate at temperatures $T \geq 10$ MeV at low densities, we evaluate the quantities τ and ω_c at the Fermi energy at temperatures $T \leq T^*$, and at the thermal energy of ultrarelativistic electrons $\tilde{\epsilon} \simeq 3T$ at $T \geq T^*$, where $T^* = T_F/3$ is the transition temperature from the non-degenerate to the degenerate regime and corresponds to the requirement that the Fermi energy becomes equal to the thermal energy of a nondegenerate gas, *i.e.*, $\epsilon_F = 3T$ [3]. It is seen that τ decreases with the temperature in the degenerate regime $T \leq T^*$ and increases in the non-degenerate regime $T \geq T^*$, which leads to a minimum at $T \sim T^*$ in the conductivity, see the next section. The temperature decrease in the degenerate regime is caused almost entirely by the structure factor $S(q)$. This is because with increasing temperature and decreasing Γ small momentum transfer scattering becomes more important which increases the effective cross-section. In the non-degenerate regime, the temperature dependence of τ is domi-

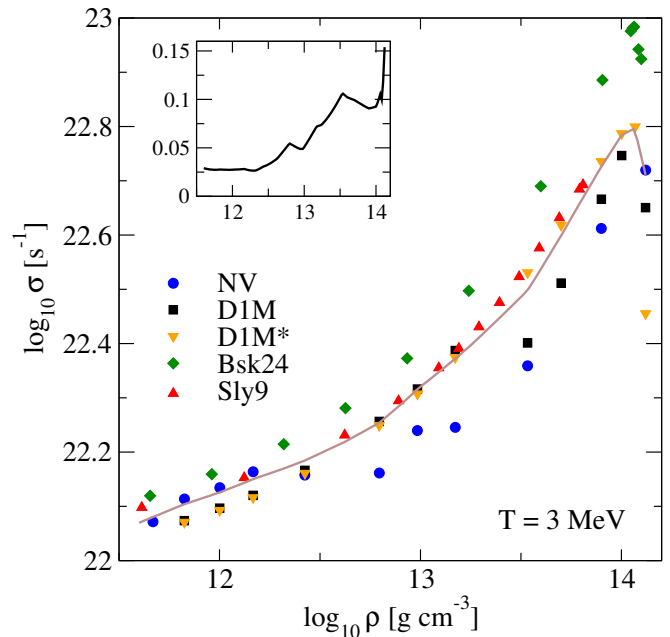


FIG. 7. Dependence of the scalar conductivity on density for five compositions. The temperature is fixed at $T = 3$ MeV. The solid line shows the logarithm of the conductivity averaged over the five compositions, and the inset shows the standard deviation for $\log \sigma$.

nated by the energy increase of electrons with temperature.

From the lower panels of Figs. 5 and 6 we see that for magnetic field $B_{12} \equiv B/(10^{12}\text{G}) = 100$ the factor $\omega_c \tau$ is close to unity at small densities and decreases slightly at high densities. This implies that the effect of anisotropy should become important at such values of fields. We see that the effects of anisotropy in the inner crust are less pronounced than in the low-density outer crust, where the anisotropy becomes important already for $B_{12} \geq 0.01$ [3].

For the anisotropy parameter, we have the scaling

$$\omega_c \tau \sim Z^{-5/3} \left(\frac{n_B - n_n}{A} \right)^{-2/3}. \quad (19)$$

It is seen that the scaling of the anisotropy parameter on the characteristics of nuclei in the inner crust differs quantitatively from the one in the outer crust $\omega_c \tau \sim Z^{-5/3} A^{2/3}$.

B. Conductivity in the low-field limit

We start with the results on the density dependence of the scalar conductivity at a fixed temperature. Figure 7 shows the scalar conductivity as a function of the density for $T = 3$ MeV. Despite the non-monotonic behavior of the relaxation time with the density, the increase of density of the states close to the Fermi surface leads to an increase of conductivity with matter density, as seen from the first formula of Eq. (16). Using this formula and the scaling of the relaxation time (18) we

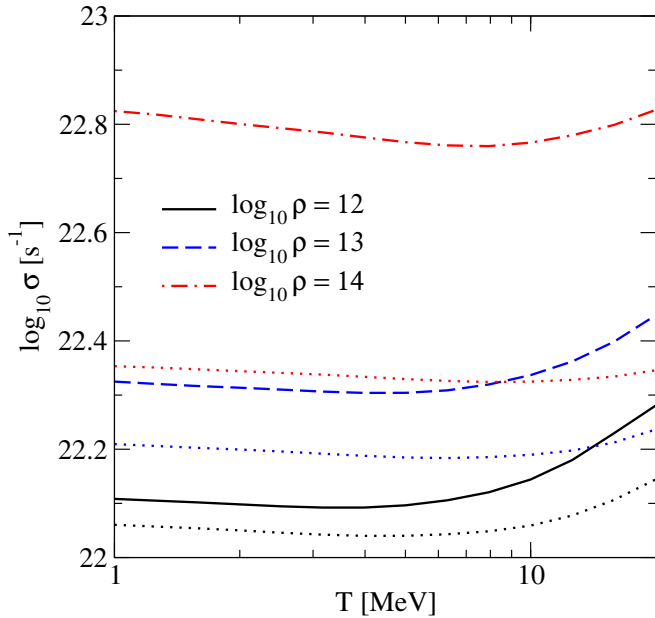


FIG. 8. The temperature dependence of the scalar conductivity for various values of the density for composition DIM*. The dotted lines show the corresponding values of σ in the case where the effect of the nuclear form factor is neglected.

find for the conductivity

$$\sigma \sim (Zn_i)^{2/3} \tau \sim Z^{-2/3} \left(\frac{n_B - n_n}{A} \right)^{1/3}. \quad (20)$$

Note that if the nuclei were symmetrical with $Z \simeq A/2$ we would have $\sigma \sim Z^{-1} \sim A^{-1}$; however this scalings do not work as nuclei are highly neutron-rich. Given that for most of the compositions Z is fixed at a (semi-magic) number, dependence of σ on the density for any given composition is controlled by the dependence of the values of A and n_n on density. Comparisons can also be made among the various compositions and the effects of various factors on the conductivity. For example, Bsk24 and DIM* compositions predict the same value of Z and n_n , therefore the differences in their conductivities can be attributed to the differences in the values of A . In addition, we show in Fig. 7 the (logarithmic) conductivity averaged over the five compositions and the standard deviation for $\log \sigma$ in the inset. As expected, the standard deviation rises with density as the differences between the compositions with regard to predicted values of Z , A , and n_n increase with density. The deviations rise sharply beyond $\log \rho [\text{g cm}^{-3}] \geq 13$, but the overall deviation remains below 10%, except close to the crust-core interface, where non-spherical nuclei are expected.

The temperature dependence of the conductivity at fixed values of the density is shown in Fig. 8. This figure allows for extrapolation to larger temperatures where the compositions of the matter used are not realistic as they have been derived at zero temperature and assuming matter without neutrinos. In the range of temperatures where the compositions are realistic $0 \leq T \leq 5$ MeV (and beyond up to 10 MeV) the temperature

dependence of the conductivity is very weak. The temperature dependence changes its slope close to T^* where the transition from the degenerate to the non-degenerate regime occurs. The actual point of the minimum is located approximately at $T \simeq 0.5T^*$.

We further investigate the effect of the finite size of the nuclei on the conductivity. Physically, the finite size of nuclei suppresses the electron-ion scattering amplitudes, which results in larger relaxation timescales and larger conductivities. The dotted lines in Fig. 8 show the corresponding values of σ in the case where the effect of nuclear form factor is neglected, *i.e.*, $F(q)$ is set to one. We clearly see from the figure that the importance of this factor increases with the density as the size of the nuclei increases with the increase of A with the density. Numerically we find that for the model DIM* the form factor increases the conductivity by factors of 1.12, 1.3, and 3 at densities $\rho = 10^{12}$, $\rho = 10^{13}$ and $\rho = 10^{14}$ g cm $^{-3}$, respectively. These factors are similar for the model DIM which predicts very large values of A at $\rho \geq 10^{13}$ g cm $^{-3}$ as well. For the rest of the models discussed, which are characterized by approximately constant values of A at $\rho \geq 10^{13}$ g cm $^{-3}$, the effect of the nuclear form factor is less pronounced at high densities, where the maximum increase of the conductivity due to the form factor is by a factor of 1.8.

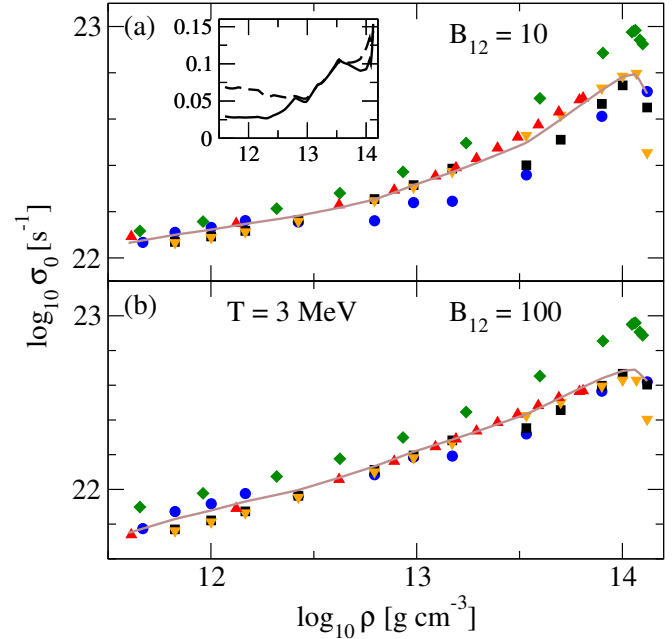


FIG. 9. Dependence of σ_0 component of the electrical conductivity tensor on density for five compositions. The labeling of the curves is as in Fig. 7. The values of the temperature and the magnetic field are indicated in the plot. The solid lines in each panel show the averages of $\log \sigma_0$ over the five compositions. The solid and dashed curves in the inset show the standard derivations of $\log \sigma_0$ for $B_{12} = 10$ and $B_{12} = 100$, respectively.

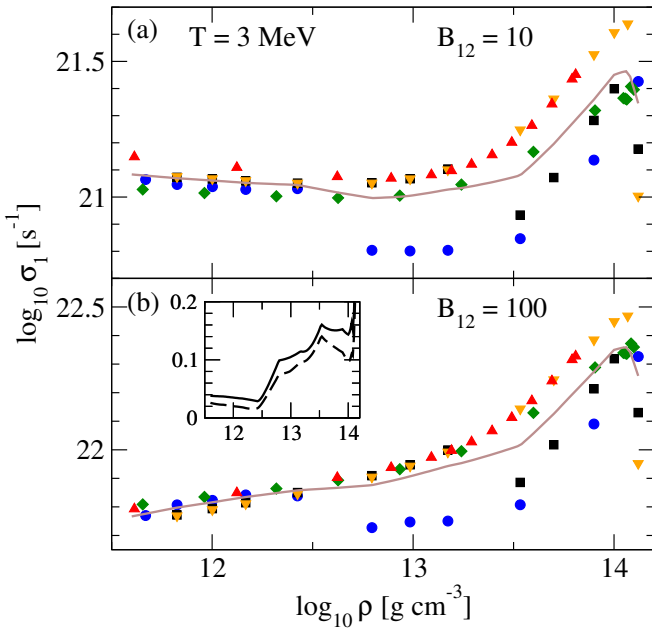


FIG. 10. Dependence of σ_1 component of the electrical conductivity tensor on density for four compositions. The labeling of the curves is as in Fig. 7. The values of the temperature and the magnetic field are indicated in the plot. The solid lines in each panel show the averages of $\log \sigma_1$ over the five compositions. The solid and dashed curves in the inset show the standard deviations of $\log \sigma_1$ for $B_{12} = 10$ and $B_{12} = 100$, respectively.

C. Conductivities in the high-field limit

We now consider the density dependence of the conductivity in the anisotropic case where the magnetic fields are large. Figure 9 shows the density dependence of the σ_0 component for two values of the magnetic field ($B_{12} = 10, 100$) for compositions considered. The temperature is fixed at $T = 3$ MeV. The same for the component σ_1 is shown in Fig. 10.

For the magnetic field $B_{12} = 10$ we have $\omega_c \tau \ll 1$ which implies essentially isotropic conduction. In this case, the component σ_0 is almost identical to the scalar conductivity σ as seen from Figs. 7 and 9, and the values of σ_1 are much lower. For $B_{12} \gtrsim 30$ the anisotropy already sets in, as can be seen from Fig. 11, and for the value $B_{12} = 100$ the transverse components of the conductivity σ_0 and σ_1 have the same order of magnitude, as already $\omega_c \tau \lesssim 1$. The scaling of the components σ_0 and σ_1 with the proton and mass number of nuclei can be easily deduced from Eqs. (16), (19) and (20). The averages of $\log \sigma_0$ and $\log \sigma_1$ and their standard deviations are also shown in Figs. 9 and 10.

We show the magnetic field dependence of the components of conductivities for fixed values of temperature and density in Fig. 11. According to Eq. (16) σ_1 is proportional to the magnetic field in the isotropic regime whereas σ_0 is independent of it; these features are seen in Fig. 11. In general, we see that the effect of the magnetic field on the conduction in the inner crust up to the limit of non-quantizing fields $B_{12} \approx 100$

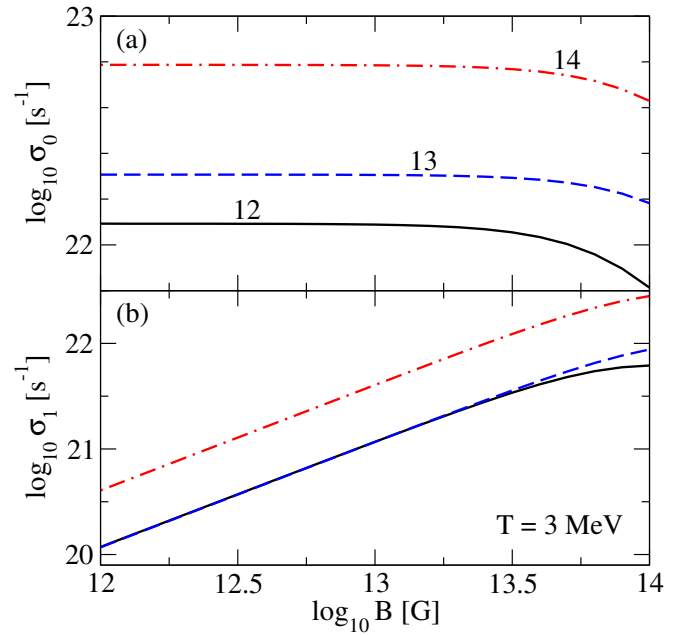


FIG. 11. The dependence of σ_0 and σ_1 components of the electrical conductivity tensor on the magnetic field at fixed temperature and for various values of the density shown on the plots for composition DIM*.

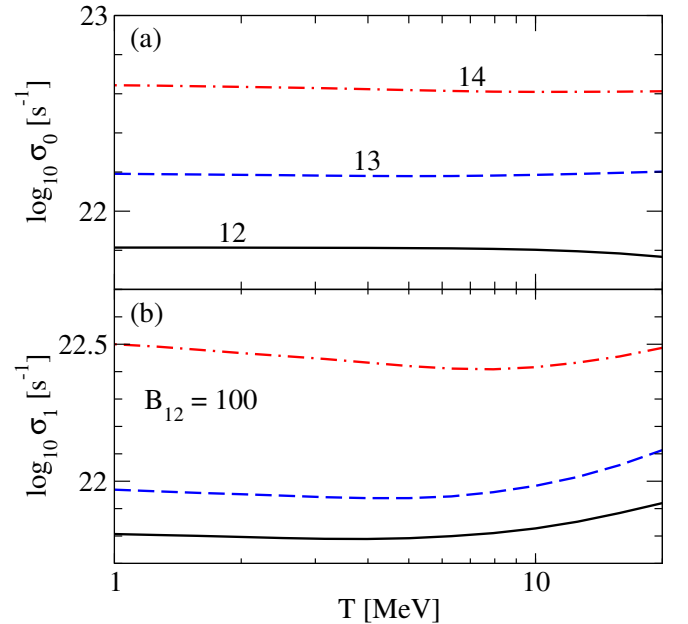


FIG. 12. The dependence of σ_0 and σ_1 components of the electrical conductivity tensor on the temperature at fixed magnetic field for various values of the density shown on the plots for composition DIM*.

is not as significant as it was the case for the outer crust, which became totally anisotropic for $B_{12} \geq 10$ [3].

The temperature dependence of the conductivity compo-

nents σ_0 and σ_1 is shown in Fig. 12 for fixed magnetic field $B_{12} = 100$. The component σ_0 is seen to be nearly independent of the temperature, because the increase in the scalar conductivity σ is almost canceled by a similar increase in the product $\omega_c\tau$, see Figs. 6 and 8. In the case of σ_1 the cancellation of these factors works partially, and there is a shallow minimum in the temperature dependence of σ_1 similar to the case of σ .

V. CONCLUSIONS

In this work, we extended the study of the finite-temperature conductivity of the outer crust of compact stars in the liquid regime in magnetic fields [3] to the inner crust characterized by a neutron drip component that forms a separate fluid. The neutron fluid affects the conductivity indirectly through the characteristics of nuclear clusters that accommodate protons and are thus the main scattering centers for electrons. The matrix element for electron scattering off the anomalous magnetic moment of a neutron (which is responsible for direct electron-neutron interaction) is by orders of magnitude smaller than the one for the Coulomb interaction. Because of higher densities, the electrons in the inner crust are mostly in the degenerate regime within the range of temperatures in which the composition of the inner crust computed at zero temperature can still be applied ($T \leq 5$ MeV). Nevertheless, our extrapolation beyond this range show that there is a minimum in the conductivity at the transition from the degenerate to the non-degenerate regime which was also the case in the outer crust. While in the degenerate regime, the conductivity is weakly dependent on the temperature, it displays a sharp rise with increasing temperature in the non-degenerate regime. Of course, a self-consistent computation of the conductivity of multi-component nuclear plasma in this regime is required to draw definitive conclusions.

To assess the uncertainties in the conductivities due to the composition we have taken an average over the five adopted compositions (NV, Bsk24, D1M, D1M* and Sly9)

and computed the standard deviation. For low magnetic fields $1 \leq B_{12} \leq 10$ the deviation is below 5% for densities $\log \rho[\text{g cm}^{-3}] \leq 12.5$ and increases up to 10% for higher densities. For larger magnetic fields the deviation can be somewhat larger, but stays below 15%. Exception are very high densities $\log \rho[\text{g cm}^{-3}] \geq 14$ where standard deviations can increase up to 20%, but one anticipates non-spherical nuclei at such densities.

The anisotropy of transport becomes sizeable for magnetic fields $B_{12} \geq 30$ and low densities as well as for larger fields $B_{12} \geq 50$ at higher densities. The field diminishes the σ_0 component of the conductivity and the non-diagonal component σ_1 becomes of the order of σ_0 at $B_{12} \approx 100$.

To conclude, we have quantified the conductivity of the warm inner crust of a compact star within the Boltzmann quasiparticle transport of electrons in the liquid phase taking into account the screening of electron-ion interaction, finite nuclear size, ion structure factor, and magnetic fields. Five different compositions were studied to assess the dependence of the results on adopted composition. In the future, this study can be extended to higher temperatures by adopting compositions that have been derived at finite temperature and account for the multi-ion composition of matter, which includes α -particles and other light clusters.

ACKNOWLEDGEMENTS

The authors gratefully acknowledge the collaborative research grant No. 97029 of Volkswagen Foundation (Hannover, Germany). We thank Mr. Jonas Dittrich for testing the code used in this work and Dr. A. Raduta for useful communications. A.S. acknowledges support through Deutsche Forschungsgemeinschaft Grant No. SE 1836/5-2, the Polish NCN Grant No. 2020/37/B/ST9/01937, and thanks the Institute for Nuclear Theory at the University of Washington for its kind hospitality, stimulating research environment, and partial support by the INT's U.S. Department of Energy grant No. DE-FG02-00ER41132.

-
- [1] A. Schmitt and P. Shternin, in *Astrophysics and Space Science Library*, edited by L. Rezzolla, P. Pizzochero, D. I. Jones, N. Rea, and I. Vidaña (Springer, New York, 2018), vol. 457 of *Astrophysics and Space Science Library*, p. 455.
 - [2] A. Y. Potekhin, J. A. Pons, and D. Page, in *The Strongest Magnetic Fields in the Universe. Series: Space Sciences Series of ISSI*, edited by V. S. Beskin, A. Balogh, M. Falanga, M. Lyutikov, S. Mereghetti, T. Piran, and R. A. Treumann (Springer, New York, 2018), vol. 54, pp. 245–297.
 - [3] A. Harutyunyan and A. Sedrakian, *Phys. Rev. C* **94**, 025805 (2016).
 - [4] A. Harutyunyan, A. Nathanail, L. Rezzolla, and A. Sedrakian, *European Physical Journal A* **54**, 191 (2018).
 - [5] J. W. Negele and D. Vautherin, *Nucl. Physics, Sect. A* **207**, 298 (1973).
 - [6] C. Mondal, X. Viñas, M. Centelles, and J. N. De, *Phys. Rev. C* **102**, 015802 (2020).
 - [7] N. Chamel, A. F. Fantina, J. M. Pearson, and S. Goriely, *Phys. Rev. C* **84**, 062802 (2011).
 - [8] A. R. Raduta and F. Gulminelli, *Nucl. Phys. A* **983**, 252 (2019).
 - [9] M. R. Pelicer, M. Antonelli, D. P. Menezes, and F. Gulminelli, *MNRAS* **521**, 743 (2023).
 - [10] A. Y. Potekhin, *A&A* **351**, 787 (1999).
 - [11] M. G. Alford, L. Bovard, M. Hanauske, L. Rezzolla, and K. Schwenzer, *Phys. Rev. Lett.* **120**, 041101 (2018).
 - [12] M. G. Alford and S. P. Harris, *Phys. Rev. C* **100**, 035803 (2019).
 - [13] M. Alford, A. Harutyunyan, and A. Sedrakian, *Phys. Rev. D* **100**, 103021 (2019).
M. Alford, A. Harutyunyan, and A. Sedrakian, *Phys. Rev. D* **104**, 103027 (2021).
M. Alford, A. Harutyunyan, and A. Sedrakian, *Particles* **3**, 500 (2020).

TABLE I. Composition NV at $B_{12} = 100$

$\log \rho$	$T = 1 \text{ MeV}$					$T = 10 \text{ MeV}$				
	$\log \tau$	$\omega_c \tau$	$\log \sigma$	$\log \sigma_0$	$\log \sigma_1$	$\log \tau$	$\omega_c \tau$	$\log \sigma$	$\log \sigma_0$	$\log \sigma_1$
11.669	-19.519	1.024	22.087	21.774	21.786	-19.537	0.872	22.123	21.762	21.805
11.825	-19.545	0.891	22.130	21.875	21.826	-19.606	0.743	22.158	21.866	21.845
12.001	-19.557	0.833	22.151	21.921	21.842	-19.639	0.689	22.176	21.913	21.861
12.167	-19.574	0.760	22.180	21.981	21.863	-19.655	0.631	22.201	21.975	21.881
12.425	-19.570	0.776	22.174	21.968	21.860	-19.651	0.644	22.196	21.962	21.877
12.795	-19.730	0.448	22.171	22.092	21.744	-19.791	0.390	22.202	22.102	21.796
12.985	-19.757	0.373	22.251	22.194	21.766	-19.817	0.325	22.271	22.202	21.807
13.173	-19.757	0.370	22.257	22.201	21.769	-19.817	0.322	22.276	22.209	21.810
13.533	-19.765	0.316	22.372	22.331	21.830	-19.826	0.274	22.380	22.333	21.854
13.900	-19.647	0.351	22.634	22.583	22.128	-19.729	0.290	22.607	22.558	22.088
14.120	-19.477	0.549	22.753	22.639	22.378	-19.590	0.424	22.702	22.602	22.300

TABLE II. Composition DIM at $B_{12} = 100$

$\log \rho$	$T = 1 \text{ MeV}$					$T = 10 \text{ MeV}$				
	$\log \tau$	$\omega_c \tau$	$\log \sigma$	$\log \sigma_0$	$\log \sigma_1$	$\log \tau$	$\omega_c \tau$	$\log \sigma$	$\log \sigma_0$	$\log \sigma_1$
11.825	-19.515	1.038	22.089	21.770	21.788	-19.530	0.884	22.128	21.757	21.808
12.001	-19.526	0.970	22.112	21.823	21.811	-19.564	0.818	22.148	21.812	21.832
12.167	-19.539	0.903	22.136	21.876	21.833	-19.600	0.753	22.168	21.866	21.854
12.425	-19.560	0.797	22.183	21.968	21.871	-19.642	0.659	22.209	21.961	21.891
12.795	-19.588	0.650	22.274	22.120	21.934	-19.668	0.541	22.290	22.115	21.951
12.985	-19.598	0.587	22.334	22.205	21.974	-19.677	0.488	22.345	22.199	21.987
13.173	-19.597	0.542	22.406	22.294	22.028	-19.678	0.449	22.410	22.286	22.034
13.533	-	-	-	-	-	-19.786	0.301	22.428	22.368	21.943
13.700	-	-	-	-	-	-19.736	0.317	22.528	22.463	22.055
13.900	-	-	-	-	-	-19.657	0.353	22.666	22.590	22.219
14.001	-	-	-	-	-	-19.612	0.378	22.737	22.652	22.308
14.120	-	-	-	-	-	-19.711	0.294	22.658	22.604	22.153

M. Alford, A. Harutyunyan, and A. Sedrakian, arXiv e-prints arXiv:2306.13591 (2023).

[14] M. G. Alford and A. Haber, Phys. Rev. C **103**, 045810 (2021).

[15] M. Alford, A. Harutyunyan, and A. Sedrakian, Particles **5**, 361 (2022).

[16] E. R. Most, A. Haber, S. P. Harris, Z. Zhang, M. G. Alford, and J. Noronha, arXiv e-prints arXiv:2207.00442 (2022).

[17] T. Celora, I. Hawke, P. C. Hammond, N. Andersson, and G. L. Comer, Phys. Rev. D **105**, 103016 (2022).

[18] S. Typel, G. Röpke, T. Klähn, D. Blaschke, and H. H. Wolter, Phys. Rev. C **81**, 015803 (2010), 0908.2344.

[19] M. Hempel, J. Schaffner-Bielich, S. Typel, and G. Röpke, Phys. Rev. C **84**, 055804 (2011), 1109.0252.

[20] M. Hempel, T. Fischer, J. Schaffner-Bielich, and M. Liebendörfer, ApJ **748**, 70 (2012), 1108.0848.

[21] X.-H. Wu, S.-B. Wang, A. Sedrakian, and G. Röpke, Journal of Low Temperature Physics **189**, 133 (2017), 1705.02525.

[22] T. Fischer, S. Typel, G. Röpke, N.-U. F. Bastian, and G. Martínez-Pinedo, Phys. Rev. C **102**, 055807 (2020), 2008.13608.

[23] A. Sedrakian, European Physical Journal A **56**, 258 (2020), 2009.00357.

[24] R. Nandkumar and C. J. Pethick, MNRAS **209**, 511 (1984).

SUPPLEMENTAL MATERIAL

TABLE III. Composition D1M* at $B_{12} = 100$

$\log \rho$	$T = 1 \text{ MeV}$					$T = 10 \text{ MeV}$				
	$\log \tau$	$\omega_c \tau$	$\log \sigma$	$\log \sigma_0$	$\log \sigma_1$	$\log \tau$	$\omega_c \tau$	$\log \sigma$	$\log \sigma_0$	$\log \sigma_1$
11.825	-19.512	1.051	22.086	21.762	21.784	-19.524	0.897	22.126	21.748	21.805
12.001	-19.524	0.981	22.108	21.814	21.807	-19.559	0.828	22.144	21.803	21.828
12.167	-19.537	0.914	22.132	21.867	21.829	-19.594	0.763	22.164	21.857	21.850
12.425	-19.558	0.807	22.177	21.959	21.866	-19.641	0.667	22.204	21.951	21.887
12.795	-19.587	0.659	22.266	22.108	21.929	-19.667	0.549	22.283	22.103	21.946
12.985	-19.595	0.598	22.325	22.191	21.969	-19.675	0.498	22.337	22.186	21.983
13.173	-19.595	0.554	22.393	22.276	22.021	-19.676	0.460	22.399	22.269	22.028
13.533	-19.545	0.547	22.554	22.439	22.178	-19.637	0.442	22.542	22.422	22.160
13.700	-19.494	0.587	22.645	22.516	22.286	-19.597	0.463	22.620	22.492	22.247
13.900	-19.417	0.663	22.769	22.610	22.433	-19.538	0.502	22.722	22.578	22.363
14.001	-19.376	0.717	22.824	22.644	22.500	-19.507	0.530	22.766	22.610	22.416
14.068	-19.357	0.753	22.838	22.643	22.520	-19.493	0.551	22.777	22.610	22.433
14.120	-	-	-	-	-	-19.757	0.312	22.487	22.420	22.018

TABLE IV. Composition Bsk24 at $B_{12} = 100$

$\log \rho$	$T = 1 \text{ MeV}$					$T = 10 \text{ MeV}$				
	$\log \tau$	$\omega_c \tau$	$\log \sigma$	$\log \sigma_0$	$\log \sigma_1$	$\log \tau$	$\omega_c \tau$	$\log \sigma$	$\log \sigma_0$	$\log \sigma_1$
11.655	-19.559	0.842	22.136	21.902	21.828	-19.631	0.701	22.159	21.894	21.845
11.962	-19.581	0.746	22.176	21.983	21.857	-19.661	0.621	22.194	21.977	21.872
12.320	-19.607	0.638	22.231	22.082	21.888	-19.684	0.535	22.244	22.077	21.901
12.627	-19.633	0.541	22.298	22.187	21.920	-19.708	0.455	22.304	22.181	21.928
12.934	-19.658	0.446	22.390	22.311	21.961	-19.732	0.377	22.388	22.303	21.960
13.240	-19.671	0.369	22.516	22.461	22.028	-19.747	0.310	22.502	22.445	22.008
13.599	-19.651	0.316	22.713	22.672	22.171	-19.735	0.260	22.677	22.639	22.113
13.905	-19.608	0.290	22.915	22.880	22.343	-19.705	0.232	22.855	22.826	22.238
14.047	-19.605	0.263	23.007	22.978	22.398	-19.706	0.209	22.938	22.915	22.274
14.056	-19.608	0.259	23.013	22.985	22.397	-19.709	0.205	22.943	22.921	22.272
14.063	-19.611	0.256	23.015	22.988	22.395	-19.711	0.203	22.946	22.924	22.270
14.085	-19.564	0.314	22.975	22.934	22.432	-19.670	0.247	22.906	22.873	22.311
14.098	-19.567	0.319	22.957	22.915	22.418	-19.671	0.250	22.889	22.856	22.302

TABLE V. Composition Sly9 at $B_{12} = 100$

$\log \rho$	$T = 1 \text{ MeV}$					$T = 10 \text{ MeV}$				
	$\log \tau$	$\omega_c \tau$	$\log \sigma$	$\log \sigma_0$	$\log \sigma_1$	$\log \tau$	$\omega_c \tau$	$\log \sigma$	$\log \sigma_0$	$\log \sigma_1$
11.613	-19.468	1.180	22.117	21.736	21.809	-19.480	0.992	22.147	21.723	21.819
12.123	-19.514	0.946	22.171	21.892	21.869	-19.588	0.775	22.194	21.882	21.880
12.623	-19.564	0.728	22.250	22.064	21.927	-19.647	0.600	22.264	22.057	21.937
12.891	-19.588	0.621	22.313	22.171	21.965	-19.670	0.515	22.320	22.164	21.971
13.091	-19.600	0.556	22.375	22.257	22.003	-19.680	0.462	22.375	22.248	22.003
13.191	-19.601	0.532	22.411	22.303	22.029	-19.682	0.440	22.408	22.292	22.024
13.291	-19.597	0.513	22.452	22.350	22.061	-19.680	0.424	22.443	22.337	22.049
13.393	-19.587	0.503	22.498	22.400	22.102	-19.673	0.413	22.484	22.383	22.081
13.491	-19.571	0.504	22.547	22.449	22.152	-19.661	0.409	22.526	22.429	22.119
13.591	-19.544	0.518	22.603	22.500	22.214	-19.640	0.415	22.573	22.474	22.168
13.691	-19.506	0.551	22.662	22.547	22.289	-19.612	0.432	22.621	22.516	22.225
13.791	-19.458	0.610	22.720	22.582	22.368	-19.576	0.465	22.664	22.547	22.285
13.809	-19.448	0.624	22.729	22.586	22.382	-19.569	0.473	22.671	22.550	22.295